

# Integrating Pore Interconnectivity and Adaptability in a Single Crystal Hierarchical Zeolite for Liquid Alkylation

Baoyu Liu<sup>1</sup>, Jiajin Huang<sup>2</sup>, Zhantu Liao<sup>2</sup>, Chongzhi Zhu<sup>3</sup>, Qiaoli Chen<sup>3</sup>, Guan Sheng<sup>4</sup>, Yihan Zhu<sup>3</sup>, Yi Huang<sup>5</sup>, and Jinxiang Dong<sup>2</sup>

<sup>1</sup>Affiliation not available

<sup>2</sup>Guangdong University of Technology - University Town Campus

<sup>3</sup>Zhejiang University of Technology

<sup>4</sup>King Abdullah University of Science and Technology

<sup>5</sup>The University of Edinburgh

April 28, 2020

## Abstract

Zeolite belongs to one of the most important families of solid acid catalysts in chemical industries. It is however severely constrained by the diffusion limitation for bulky molecules, the lack of multi-functionality for sequential reactions and pore adaptability towards specific adsorbates, due to the small micropore size and simple aluminosilicate framework. Introducing mesopores into the zeolitic framework towards hierarchical zeolites is prevailing, but usually suffers from compromised crystallinity as well as insufficient interconnectivity and openness of mesopores. Herein, a novel of acid-redox co-functionalized single-crystalline zeolite with highly open and interconnected mesopores is designed and fabricated. As a proof-of-concept study, we integrate the solid acid and Fe-oxy redox sites in a hierarchical MEL zeolite with well characterized microporosity and mesoporosity. It exhibits superior activity and stability towards the alkylation between mesitylene with benzyl alcohol, arising from greatly facilitated intracrystalline molecular diffusion, mitigated metal leaching and optimized adsorbate-pore wall interactions.

## 1. Introduction

The alkylation of mesitylene with benzyl alcohol is an important reaction to produce the valuable chemicals for aviation fuel additive reagents, dyes, pharmaceuticals, electrolytes and cosmetics.<sup>1,2</sup> However, this reaction is traditionally catalyzed by homogeneous catalysts such as  $\text{AlCl}_3$ ,  $\text{H}_2\text{SO}_4$  and  $\text{BF}_3$ ,<sup>3,4</sup> which cause many problems like pollution, corrosion and separation.<sup>5</sup> Heterogeneous solid acid catalysts, especially zeolites with a versatile solid acid and tunable architecture, are highly desired towards a “green” approach for the alkylation of mesitylene.<sup>6</sup> A major concern for conventional zeolite lies in the severe diffusion limitation arising from the small pore size and the rigorous coking problem.<sup>7</sup> Hierarchical zeolites with both microporosity and mesoporosity should have in principle largely circumvented diffusion limitation.<sup>8-11</sup> However, those with polycrystalline mesopore walls would usually have compromised framework acidity and stability.<sup>12</sup> Hierarchical single-crystalline zeolites well retain these properties,<sup>13-15</sup> while the “quality” (i.e. the interconnectivity and surface openness) of the intracrystalline mesopores remains largely unevaluated and those constricted or closed ones are totally inaccessible for bulky molecules.<sup>16,17</sup>

Another important but usually lacking structural feature for the complex porous network of hierarchical zeolites is the adsorbate-specific pore adaptability, which allows further control of product selectivity through largely differentiated adsorbate-pore wall interactions. In addition, it is widely reported that monofunctional acid sites in the zeolite framework exhibit poor activity towards the alkylation of aromatics.<sup>18,19</sup> The redox

transition metal additives, such as Fe, Co and Pt, significantly improve the activity of benzylation.<sup>20</sup> These metal species are usually loaded on the external surfaces of zeolites and in the form of particles, leading to severe sintering and leaching issues.<sup>21</sup> Immobilizing metal species into zeolite matrix is an effective method to mitigate these problems, but is unavailable for conventional chemical synthesis as metal precursors can hardly undergo co-condensation with zeolite precursors instead of forming the oxyhydroxide precipitates under the conditions for zeolite synthesis.<sup>22</sup>

In present research, we developed a simple and general strategy to fabricate a hierarchical single-crystalline MEL zeolite co-functionalized with both solid acid and Fe-oxy redox sites. The Fe species were immobilized into silicate-2 with the assistance of ligands-stabilized iron cations. The subsequent orientated crystal transformation was then accompanied by a targeted leaching-hydrolysis process that finally converted the Fe-containing silicate-2 into the acid-redox co-functionalized single crystalline mesoporous MEL zeolites. The single-crystalline/bi-functionalized microporous framework as well as the highly open/interconnected mesoporosity of the MEL zeolite were unambiguously determined and evaluated by a complementary combination of high-resolution transmission electron microscopy (HRTEM), electron tomography (ET) and positron annihilation lifetime spectroscopy (PALS). The kinetic adsorption experiment further validated the pore adaptability towards non-polar adsorbates. These unique structural features all together lead to greatly facilitated intracrystalline molecular diffusion, mitigated metal leaching and optimized adsorbate-pore wall interactions towards an excellent overall catalytic performance for the alkylation of aromatics.

## 2. Experimental section

### 2.1 Materials

The reagents used in this synthesis process were tetraethyl orthosilicate (TEOS, analytical grade, Damao Chemical Reagent Factory, China), tetrabutylammonium hydroxide (TBAOH, 40 wt % aqueous solution, Energy Chemical, China), aluminum isopropoxide (analytical grade, Aladdin), iron citrate (analytical grade, Aladdin), iron (III) chloride (Adamas-beta), benzyl alcohol (analytical grade, Damao Chemical Reagent Factory, China), and 1,3,5-trimethylbenzene (analytical grade, Aladdin). All water in the experiment was deionized water.

### 2.2 Catalyst preparation

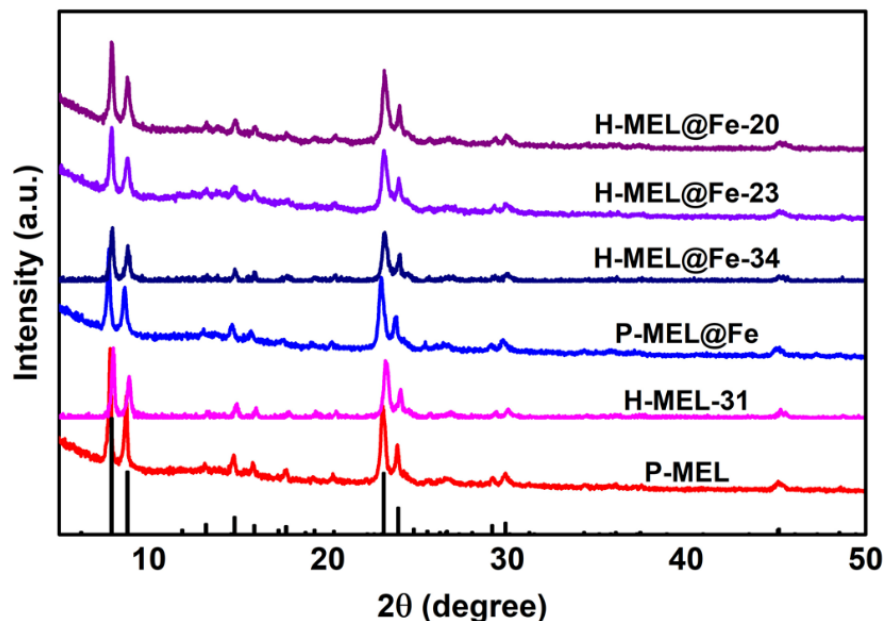
Pure silica MEL and Pure silica Fe containing MEL zeolites were synthesized by hydrothermal method, using TEOS as a silicon source, iron citrate as the iron source and TBAOH as the organic template, respectively. Typically, the TEOS was slowly added to TBAOH solution under vigorous stirring, and after mixing at room temperature for 3 hours, iron citrate and deionized water were added. The final molar composition of the gel was 1 TEOS : 0.25 TBAOH : 25 H<sub>2</sub>O : x Fe<sub>2</sub>O<sub>3</sub> (x = 0 and 0.007, respectively). After aging for 6 hours at 30 °C, the prepared mixture was placed into stainless steel autoclave and crystallized at 170 °C for 72 hours under static conditions. After crystallization, the product was filtered, washed several times with deionized water, and dried overnight at 100°C. Finally, the organic templates were removed by calcination at 550 °C for 6 hours in an air atmosphere. Those samples were denoted as P-MEL (pure silica MEL zeolite) and P-MEL@Fe (Pure silica Fe containing MEL zeolite), respectively.

The above synthesized P-MEL and P-MEL@Fe samples were further treated. Typically, a certain amount of aluminum isopropoxide was dissolved in 0.1 M/L of TBAOH solution, and then the concentration of aluminum isopropoxide solution was tuned to 0.015 M/L, 0.024 M/L and 0.03 M/L, respectively. The amount of solution was 30 ml/g as-prepared P-MEL or P-MEL@Fe. Then, it was placed into a stainless-steel autoclave and crystallized at 170 °C for 72 hours under static conditions. In the same way, the product was filtered, washed several times with deionized water, and dried overnight at 100°C. Finally, the organic template was removed by calcination at 550 °C for 6 hours in an air atmosphere. Those hierarchical zeolites were denoted as H-MEL-31 (it was obtained from P-MEL and the Si/Al = 31) or H-MEL@Fe-34, H-MEL@Fe-23 and H-MEL@Fe-20 (they were prepared from P-MEL@Fe and the Si/Al = 34, 23 and 20), respectively. The corresponding Si/Al ratios of zeolites were determined by ICP-OES.

### 3. Results and discussion

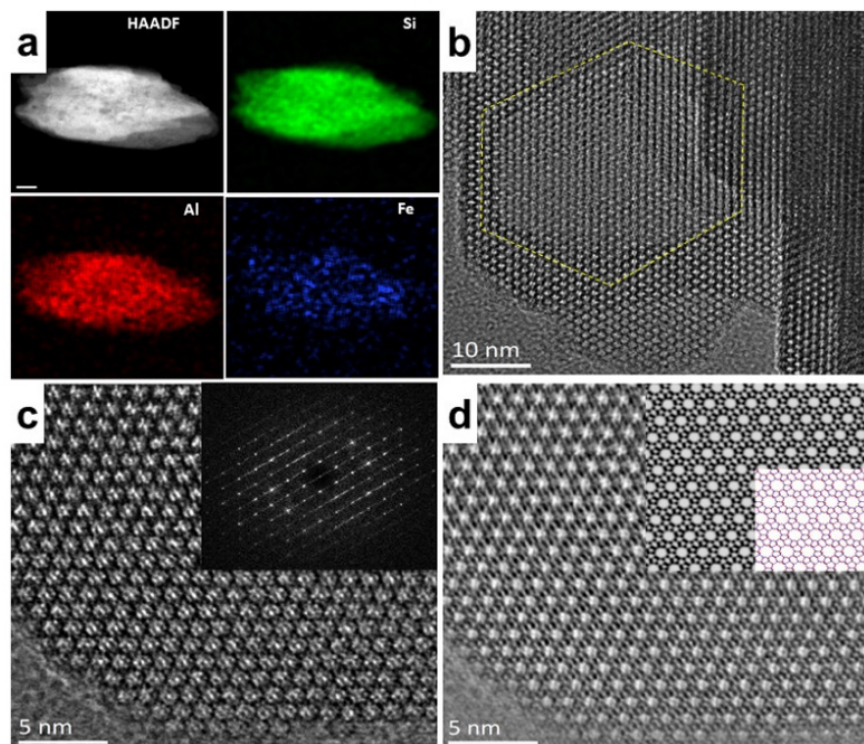
#### 3.1 Characterization of zeolites

Fig. 1 showed the powder X-Ray Diffraction (XRD) patterns of various MEL zeolite samples, it was observed that all the synthesized samples exhibited the characteristic peaks (such as  $2\theta = 7.9^\circ, 8.8^\circ, 14.8^\circ, 23.1^\circ$  and  $23.9^\circ$ ) of MEL topologic framework,<sup>23,24</sup> indicating that the MEL zeolites were successfully fabricated in present work. No other detectable diffraction peaks for metal phases, such as large iron oxides, were found, which meant the substantial absence of large metal crystallites. In addition, the EDX mapping (Fig. 2a) further demonstrated that the immobilized Fe species were homogeneously distributed throughout the whole MEL zeolite particle.



**Figure 1** . XRD patterns of different MEL zeolite samples.

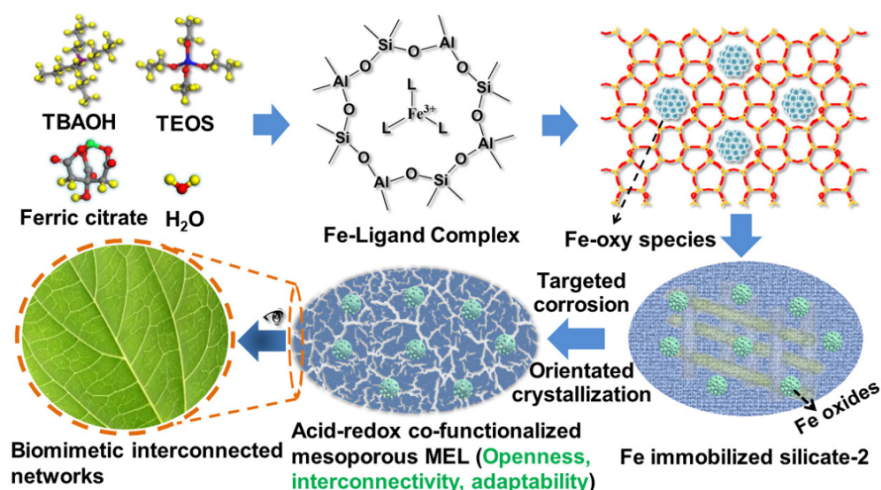
The chemical state of these species was characterized by XPS, and the results were displayed in Fig. S1. For Fe containing MEL zeolites, two peaks at 711.8 and 725.4 eV were observed corresponding  $\text{Fe}_{2p_{3/2}}$  and  $\text{Fe}_{2p_{1/2}}$  in  $\text{Fe}^{3+}$ , respectively.<sup>25,26</sup> Moreover, the additional satellite peaks at  $\sim 716.3$  eV and  $729.9$  eV can also be observed in P-MEL@Fe (Fig. S1a) and H-MEL@Fe- $x$  (Fig. S1b-S1d), which represented the binding energy of  $\text{Fe}_{2p_{3/2}}$  and  $\text{Fe}_{2p_{1/2}}$  in Fe(III) of  $\text{Fe}_2\text{O}_3$ .<sup>27</sup> The UV-vis spectroscopy of resultant zeolite samples was given in Fig. S2, and the corresponding percentages of different iron species of zeolites were listed in Table S1, it was found that  $\text{Fe}^{3+}$  species occupied the majority. Moreover, The EPR analysis was further carried out to detect the structure and coordination environment of Fe species in Fe-containing MEL zeolites, where the two distinct resonance signals at  $g = 4.3$  and  $2.0$  referred to  $\text{Fe}^{3+}$  species in a distorted tetrahedral and a highly symmetric coordination respectively (Fig. S3).<sup>28,29</sup> Based on the above analysis, it deduced that most of iron species loaded in the P-MEL@Fe, H-MEL@Fe-34, H-MEL@Fe-23 and H-MEL@Fe-20 samples existed in the form of Fe(III).



**Figure 2.** (a) HAADF-STEM image and elemental distributions of H-MEL@Fe-20 by EDS mapping. HRTEM image of the single-crystalline hierarchical H-MEL@Fe-20 zeolite (b) containing faceted intracrystalline mesopores, and (c) containing pore walls along [100] direction. FFT pattern is embedded. (d) Contrast-transfer-function (CTF) corrected image (at a defocus of -230 nm) with overlaid simulated projected potential map (with a point-spread-function width of 1.8 Å) and structural projections of H-MEL-31 zeolite along [100] direction.

SEM images of as-synthesized MEL zeolites showed a uniform rugby-like morphology (Fig. S4), and P-MEL had a smooth surface. When Fe and Al species were incorporated into the zeolite framework, the samples exhibited a rough surface and some fragments appeared on the surface of zeolites (Fig. S4b-S4f), but the rugby-like structure was not destroyed. TEM images of zeolites were further carried out to investigate the framework structure of samples, as shown in Fig. S5. It was observed that P-MEL (Fig. S5a) and P-MEL@Fe (Fig. S5c) showed condensed structure, while the H-MEL-31 and H-MEL@Fe-*x* exhibited unconsolidated structure (Fig. S5b and S5d-S5f). Besides, electron diffraction pattern of a randomly selected MEL zeolite particle further confirmed its single-crystalline nature (Fig. S6).

The N<sub>2</sub> adsorption-desorption isotherm was used to reveal the porosity of resultant MEL zeolites, as shown in Fig. S7. It was observed that H-MEL-31, H-MEL@Fe-34, H-MEL@Fe-23 and H-MEL@Fe-20 showed distinct Type-IV isotherms with H2 hysteresis loop corresponding to capillary condensation in the mesopores.<sup>30,31</sup> By contrast, the P-MEL and P-MEL@Fe didn't show any hysteresis loops owing to sole microspore. The pore size distribution of obtained zeolite samples was analyzed by NLDFT (non-local density functional theory) and BJH (Barrett-Joyner-Halenda) methods respectively, and the data was shown in Fig. S8. All of samples exhibited a narrow peak at ~0.56 nm in Fig. S8a corresponding microspore size of MEL zeolite, while the H-MEL-31, H-MEL@Fe-34, H-MEL@Fe-23 and H-MEL@Fe-20 showed the additional broad peaks in Fig. S8b compared with P-MEL.



**Scheme 1** . Synthetic Strategy for Fe immobilized hierarchical single-crystalline MEL zeolites.

and P-MEL@Fe in the region of 3~4.5 nm, which were attributed to the formation of mesoporous. The above TEM images, N<sub>2</sub> adsorption data combined with textural properties of zeolites (Table S2) verified that the H-MEL-31 and H-MEL@Fe-*x*zeolites encompassed a significant amount of mesoporosity, possibly arising from the orientated crystal transformation process: i) the silica source (TEOS) and template (TBAOH) assembled with Ferric citrate through the electrostatic and dispersion interactions between zeolite precursor and solvated ligand-stabilized Fe species<sup>22</sup>, inducing the formation of Fe containing silicate-2; ii) these Fe containing silicate-2 underwent the targeted corrosion towards silicon extraction by interactions between Si-OH groups on the surface of silicate-2 and TBA<sup>+</sup>, resulting in the generation of voids in the silicate-2<sup>32</sup>. Simultaneously, the Fe containing silicate-2 finished crystal transformation *via* directional control of crystallization process combined with leached silicate oligomers and additional aluminum isopropoxide species, guiding the formation of acid-redox co-functionalized single crystalline mesoporous MEL zeolites, as schematically illustrated in Scheme 1. These mesopores were enclosed by a series of low-index facets like [011] and [010] as clearly observed in HRTEM images from an “edge-on” projection (Fig. 2b and 2c). After correcting the defocus effects (Fig. 2d), The HRTEM images of the crystalline pore walls also well matched the simulated projected potential and structural projections of a MEL zeolite along the [100] direction.

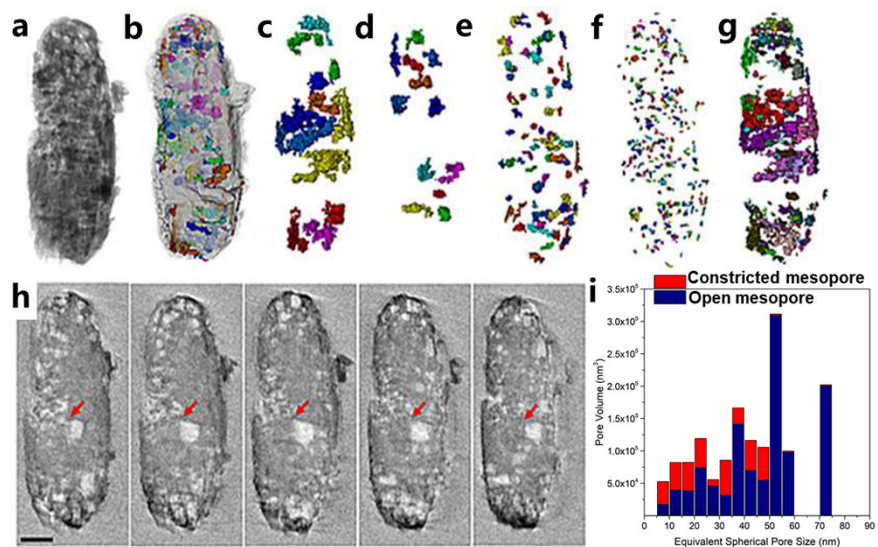


**Figure 3 .** (a) Reconstructed volume by electron tomography, (b) Volume with labelled mesopores embedded and rendered in diverse colors, (c-f) Labelled mesopores classified by different mesopore volume (from left to right:  $> 3 \times 10^4 \text{nm}^3$ ,  $1 \sim 3 \times 10^4 \text{nm}^3$ ,  $1 \sim 10 \times 10^3 \text{nm}^3$  and  $1 \sim 10 \times 10^3 \text{nm}^3$ ), (g) mesopores open to the surface and (h) sequential slices of the reconstructed volume with an interval of 10 nm for H-MEL-31; the red arrow shows the mesopore interconnectivity among slices (i) A statistical analysis of mesopore volume distribution over different equivalent spherical pore size. Red and blue bars refer to constricted/closed and open mesopores respectively.

The “quality” of these intracrystalline mesoporosity, in terms of interconnectivity and openness, can be directly evaluated in three-dimensions and real-space by ET. Based on a TEM tilt series of H-MEL-31 as a typical mesoporous MEL zeolite, the reconstructed 3D tomogram can be visualized through volume rendering in Fig. 3a and Fig. S9. From the 3D tomogram, the intracrystalline mesoporosity can be directly identified, which could even be more clearly observed from sequential slices of the tomogram as shown in Fig. 3h. These slices with an interval of 10 nm exhibited highly interconnected voids either within or between individual slices, implying a high degree of 3D interconnectivity of mesopores. A thorough segmentation of the tomogram allowed the precise labeling in 3D of individual interconnected mesopores with different size and shape as shown in Fig. 3b-3f (rendered with different colors). These labelled mesopores can be further classified according to their different equivalent spherical pore size and quantified statistically in a bar chart as shown in Fig. 3i. Among these mesopores, those connected to the surface can be further labelled and quantified as shown in Fig. 3g & 3i, which were defined as “open mesopores” (otherwise “constricted” or “closed” ones). Accordingly, it can be observed that majority of the interconnected intracrystalline mesopores were highly open to the surface (Fig. 3i). Moreover, the positron annihilation lifetime spectroscopy (PALS) was further employed to verify the pore connectivity of zeolites

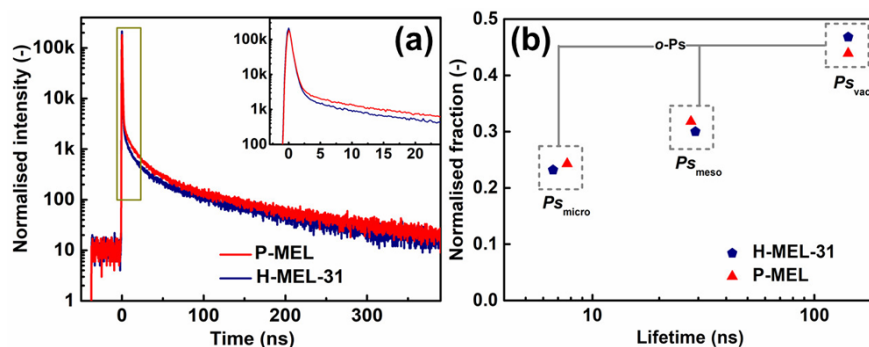


**Figure 4 .** (a) Positron annihilation lifetime spectroscopy lifetime spectra and (b) corresponding lifetime components and relative fractions for P-MEL and H-MEL-31 zeolites.

due to its unprecedented sensitivity towards bulk connectivity of the complex pore network. The normalized PALS spectra and corresponding lifetime components with relative fractions of P-MEL and H-MEL-31 were shown in Fig. 4a and Fig. 4b, respectively. It was observed from Fig. 4b that the P-MEL exhibited higher fractions of o-Ps annihilating in the micro- and mesopores than H-MEL-31, which was indicative of increased resistance of o-Ps migration from both micropores-to-mesopores and micropores/mesopores-to-vacuum.<sup>16</sup> While the high fraction of o-Ps annihilating in vacuum for the hierarchically structured H-MEL-31 compared with P-MEL suggested that H-MEL-31 possessed superior interconnectivity of the micro- and mesopore network and surface openness, which greatly promote the intracrystalline molecular transport.<sup>17</sup>

### 3.2 Acidity of zeolites

In general, the acidity of zeolites is from the Al species that are substituting for tetrahedral Si atoms in the framework, which gives the Brønsted acid sites and Lewis acid sites depending on different Al coordinated environment.<sup>33</sup> For MEL zeolite, it contains 7 crystallographically distinct T sites, as shown in Fig. 5 and

Fig. S10. Here, the acidity of synthesized samples was evaluated by IR spectra of pyridine/2,6-di-tert-butyl pyridine adsorption on H<sup>+</sup> form of zeolites. The pyridine with a kinetic diameter of  $\sim 0.5$  nm can enter the channel of MEL ( $0.53 \times 0.54$  nm).<sup>34</sup> Thus, it can detect the total acidity of zeolites. Fig. S11a exhibited the IR spectra of adsorbed pyridine over the investigated samples, it was known that the absorption bands at  $\sim 1546$  and  $1446$  cm<sup>-1</sup> were attributed to Brønsted acid sites and Lewis acid sites, respectively,<sup>35,36</sup> and the corresponding acidity of zeolites were listed in Table S3. As can be seen from Table S3, P-MEL and P-MEL@Fe didn't have any Brønsted acidity due to the absence of Al species in the framework of MEL zeolites. After incorporating Al into the zeolite lattice, the Brønsted acidity of samples gradually increased. For example, the Brønsted acidity of P-MEL@Fe and H-MEL@Fe-*x* increased in the order of P-MEL@Fe < H-MEL@Fe-34 < H-MEL@Fe-23 < H-MEL@Fe-20, which indicated that Al species were preferred to exist in the form of Si-OH<sup>+</sup>-Al, resulting in the generation of Brønsted acid sites. In addition, P-MEL@Fe showed a higher Lewis acidity than that of P-MEL owing to the additional Fe species that can become the Lewis acid sites by accepting a pair of electrons from the adsorbed species.<sup>37</sup>

2,6-di-tert-butyl pyridine (2,6-DTBPY) with a kinetic diameter of  $\sim 0.8$  nm was difficult to enter the channel of MEL zeolite, and therefore it can be used to test the acidity on the external surface of zeolites. As shown in Fig. S11b, the band at  $\sim 1616$  cm<sup>-1</sup> was characteristic of Brønsted acid sites, which can catalyze the alkylation between mesitylene (the kinetic diameter of  $\sim 0.87$  nm) and benzyl alcohol. Table S3 gave the external Brønsted acidity of zeolites, it was observed that P-MEL and P-MEL@Fe didn't show any external Brønsted acidity owing to the missing of Al species. However, the concentration of Brønsted acid of H-MEL@Fe-*x* on the external surface increased with decreasing Si/Al ratios, and the Brønsted acid/Lewis acid ratios of H-MEL@Fe-*x* with Si/Al ratios also exhibited the similar trend, indicating that the Brønsted acid/Lewis acid ratios and external Brønsted acidity of H-MEL@Fe-*x* can be modulated by tuning the Si/Al ratios of zeolites, which is important for tailoring the catalytic properties of zeolite catalysts.

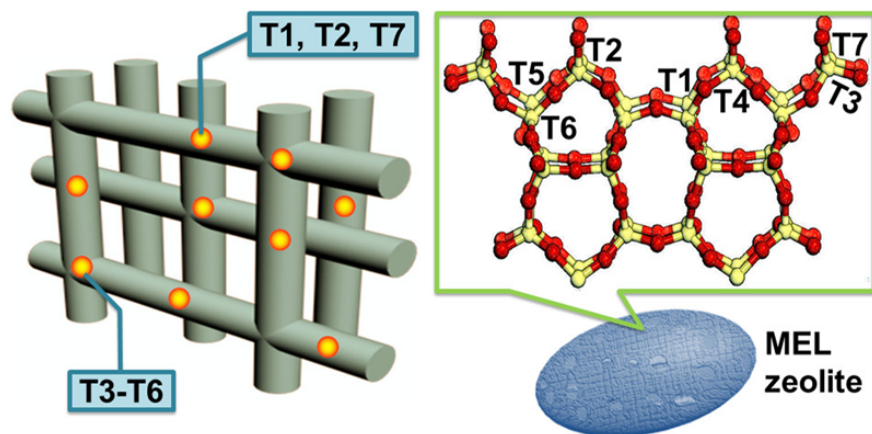


**Figure 5** . The crystal structure model of various T-sites in MEL lattice.

### 3.3 Analysis of diffusion

Over the above the effects arising from pore size, pore interconnectivity and surface openness, the chemical environment of the internal pore wall also plays a critical role determining the overall molecular diffusion properties. The kinetic adsorption experiments over diverse probe molecules allow the unambiguous discrimination between intracrystalline and surface diffusion events.<sup>38</sup> Hereby, the effects arising from electrostatic interaction between internal/external surface and adsorbate were investigated over the non-polar benzene and polar toluene molecules with a similar kinetic diameter ( $\sim 0.56$  nm) close to the channel size of MEL ( $0.53 \times 0.54$  nm) respectively. These two selected probe molecules were also free of functional groups to avoid any potential chemical bonding with the surface. Fig. 6(a,b) showed the plots of transient fractional uptake  $[(Q_t - Q_0)/(Q_e - Q_0)]$  of benzene and toluene versus square root of time in H-MEL-31, P-MEL@Fe and

H-MEL@Fe-20 at 35 °C, respectively. Briefly, the logarithm of normalized transient fractional uptake  $[(Q_t - Q_0)/(Q_e - Q_0)]$  versus square root of time produce a straight line in a short time period. The slope of the kinetic adsorption curve can be used to calculate the diffusion time constant ( $D/r_2$ ), which is based on the Fick's law (see Supporting Information) and summarized in Table S4. It was found that the diffusion time constants ( $D/r_2$ ) for all investigated samples were well within the scale of  $10^{-3} \text{ s}^{-1}$ , indicating that the diffusion process in these as-synthesized MEL zeolites was dominated by a combination of both intracrystalline and surface diffusion.<sup>39,40</sup>

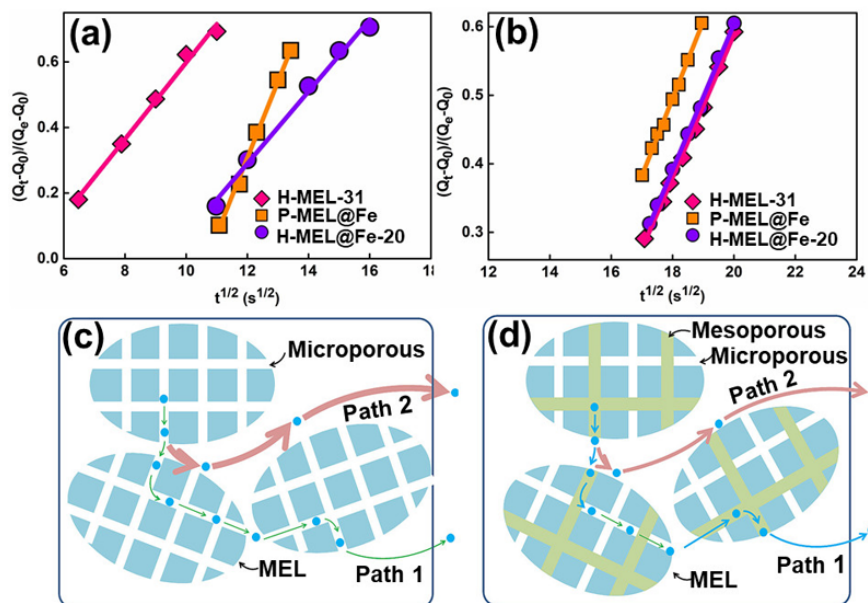


**Figure 6** . Plots of the fractional adsorption uptakes  $[(Q_t - Q_0)/(Q_e - Q_0)]$  of benzene (a), toluene (b) against the square root of adsorption time, and proposed diffusion path of benzene/toluene molecules during adsorption over (c) P-MEL@Fe and (d) H-MEL-31/H-MEL@Fe-20 samples.

Schematic illustrations of these two distinct diffusion pathways (i.e. path 1: intracrystalline diffusion; path 2: surface diffusion) over either conventional or hierarchical MEL zeolites were shown in Fig. 6c and Fig. 6d, respectively. In general, the surface diffusion is much faster than intracrystalline diffusion that is performed through the complicated porous network due to the limited mass transport. For P-MEL@Fe with solely micropores (Fig. 6c), molecular diffusion across the external surface of MEL zeolites (path 2) dominated, together with a larger  $D/r_2$  value, as shown in Table S4. For hierarchical H-MEL-31 and H-MEL@Fe-20 zeolites with highly interconnected and open mesopores (Fig. 6d), the intracrystalline molecular diffusion (path 1) was largely promoted along with a reduced  $D/r_2$  value (Table S4). Interestingly, such a marked difference in molecular diffusion between conventional and hierarchical MEL zeolites over the non-polar benzene was totally absent for experiments carried out over the polar toluene, where enhanced surface diffusion and a larger  $D/r_2$  value was observed. This indicated that the chemical environment of the internal pore walls of hierarchical MEL zeolites favored the interaction with non-polar adsorbates and associated intracrystalline molecular diffusion.

### 3.4 Catalytic activity

In order to evaluate the catalytic performance of resultant MEL zeolites, the alkylation of mesitylene with benzyl alcohol was carried out, which is an important reaction for the production of fine chemicals and pharmaceutical intermediates.<sup>1</sup> According to the previous reports,<sup>41,42</sup> the kinetic diameter of mesitylene (0.87 nm) is obviously larger than the micropore size of MEL zeolite. For the liquid benzylation of mesitylene,<sup>5</sup>

it is well known that both the alkylation of mesitylene as the target reaction and self-etherification of benzyl alcohol as a side reaction can be catalyzed by either Lewis or Brønsted acid sites throughout the internal/external surfaces of (hierarchical) MEL zeolite. Thus, the alkylation reaction between mesitylene with benzyl alcohol takes place exclusively on the external surface of conventional microporous MEL zeolite particles, while self-etherification occurs on both external surface and the much more abundant internal surface of pore walls simultaneously. On the contrary, the hierarchical single-crystalline MEL zeolite adopts highly open and interconnected mesopores, which allows the intracrystalline diffusion of the bulky mesitylene molecules. As shown in Fig. 7a, for the P-MEL zeolite, no conversion of benzyl alcohol was observed after 20 h, indicating that P-MEL didn't have any activity in alkylation reaction owing to the absence of acidity. While H-MEL-31 showed an increasing conversion of benzyl alcohol with time on stream, suggesting that the acid sites were active species. Interesting, the integration of both solid acid and Fe-oxy redox sites in such a hierarchical MEL zeolite could further enhanced the activity against benzyl alcohol, due to the involvement of  $\text{Fe}^{3+}/\text{Fe}^{2+}$  redox pairs in the well-accepted redox mechanism for benzylation of mesitylene (Scheme S1).<sup>20</sup>

From the perspective of product selectivity, the target product 2-benzyl-1,3,5-trimethylbenzene (BTMB) from the benzylation of mesitylene was greatly favored over the hierarchical H-MEL-31 zeolite together with an inhibited self-etherification side reaction that produced dibenzyl ether (Fig. 7b). The explanation was straightforward and two-fold: i) the highly open and interconnected mesopores with large surface areas accommodated the bulky mesitylene and BTMB molecules so as to promote the target alkylation reaction; ii) the remarkably decreased affinity of pore walls to polar adsorbates further reduced the concentration of benzyl alcohol in the porous network and inhibited the self-etherification side reaction. Notably, based on the reaction cycles<sup>20</sup> (Fig. 7c) and the much faster self-etherification side reaction, a short "induction period" with a low BTMB selectivity was observed before the quasi-equilibrium steady state was reached, when dibenzyl ether also worked as an alkylating agent<sup>3</sup> towards a high and stable BTMB selectivity (Fig. S12). Interestingly, we observed a decrease in BTMB selectivity for the acid-redox co-functionalized MEL zeolite despite the significantly increased conversion of benzyl alcohol (Fig. 7b, Fig. S13 and Fig. S14). As we all known that Fe-containing solid catalysts possessed redox properties ( $\text{Fe}^{3+} + \text{e}^- \rightarrow \text{Fe}^{2+}$ ), which dominated the benzylation reaction regardless of catalysts acidity.<sup>19</sup> In other words, the incorporation of  $\text{Fe}^{3+}$  species in the zeolite framework greatly enhanced the activity of benzyl alcohol, resulting in the formation of benzyl carbocation, which was quickly transformed into dibenzyl ether. However, the dibenzyl ether must be hydrolyzed to form benzyl alcohol, and then it can participate in the alkylation with mesitylene to produce BTMB. But the hydrolysis rate of dibenzyl ether was considered to be slower than the generation of dibenzyl ether,<sup>43</sup> leading to the accumulation of dibenzyl ether, which reduced the selectivity of BTMB for Fe containing MEL zeolites. The whole transformation process of benzyl carbocation was depicted in Fig. 7d, which clearly illustrated the transition pathway of benzyl carbocation arising from the activation of benzyl alcohol over combined solid acid and redox sites.<sup>44</sup> In addition, a leaching test of typical catalyst corroborated that the acid-redox co-functionalized MEL zeolites exhibited excellent stability against metal leaching (Fig. S15).

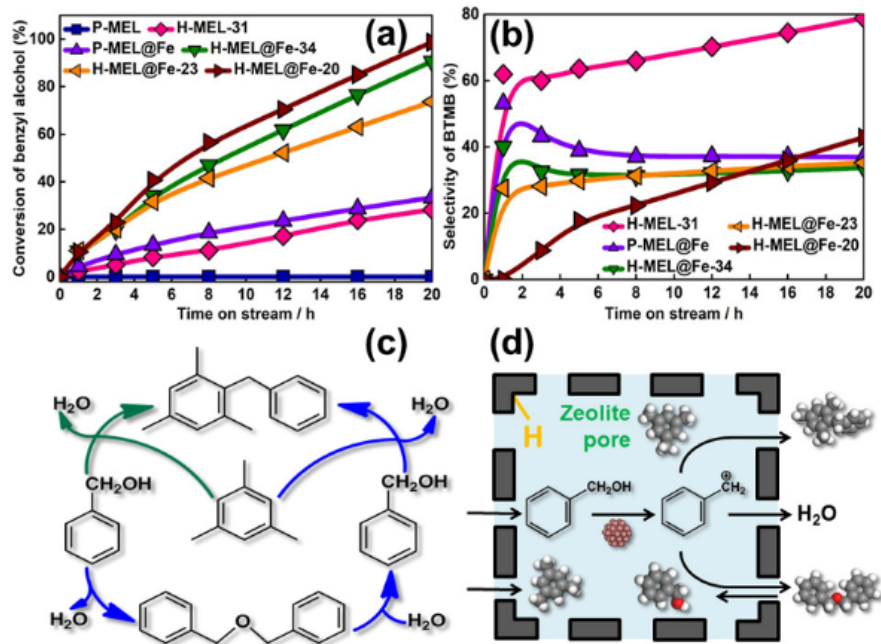


**Figure 7.** (a) Conversion of benzyl alcohol and (b) selectivity of BTMB with time-on-stream on synthesized zeolites; (c) the proposed reaction networks and (d) scheme showing the transformation of benzyl carbocation.

### 3.5 Coke analysis

A part of spent catalysts was taken for thermogravimetric analysis (TGA) to investigate the coke formed in MEL zeolites. Fig. S16 showed the weight loss curves of spent H-MEL-31, P-MEL@Fe and H-MEL@Fe-20 samples, which exhibited three distinct regions of weight loss for all of samples in temperature ranges of 25-150°C, 150-350°C and 350-700°C, respectively. Generally, the weight loss below 150°C was attributed to the moisture and adsorbed water in zeolite cavities and channels.<sup>45</sup> The mass loss observed in the temperature range of 150-350 °C was assigned to soft coke that occurred at a moderate temperature and can be extracted by organic solvent,<sup>46</sup> and the weight loss of H-MEL-31, P-MEL@Fe and H-MEL@Fe-20 in the temperature range of 350-700°C can be classified as hard coke or insoluble coke. It was worth noting that the proportion of hard coke in the total coke for H-MEL-31, P-MEL@Fe and H-MEL@Fe-20 was about 35 %, 27% and 48 %, respectively. Therefore, we deduced that the coke formed during the alkylation of mesitylene with benzyl alcohol over the investigated MEL zeolite catalysts was mainly soft coke.<sup>47</sup>

To further investigate the composition of the soluble coke on the used catalyst, the soft coke in H-MEL-31, P-MEL@Fe and H-MEL@Fe-20 were extracted by 1,3,5-trimethylcyclohexane and subsequently were analyzed by GC-MS,<sup>47,48</sup> as shown in Fig. S17. It was observed that these soft cokes were mainly composed of raw materials, solvents, products and internal standard substances (dodecane), the polyaromatics and multi-methybenzenes were not detected, which was in agreement with the TGA analysis that the main coke was soluble coke.

## 4. Conclusions

In summary, we propose here a simple and general strategy to fabricate acid-redox co-functionalized hierarchical single crystal MEL zeolites with well-evaluated mesoporosity, in terms of surface openness, pore interconnectivity and adsorbate-specific pore adaptability. This strategy works well on a hierarchical MEL zeolite system that simultaneously integrates solid acid and Fe-oxy redox sites, which exhibits greatly enhanced catalytic activity and stability towards benzylation of mesitylene. Mechanistic insights are provided that the superior catalytic performance originates from the enhanced intracrystalline molecular diffusion,

mitigated metal leaching and optimized adsorbate-pore wall interactions.

## Associated content

## Supporting Information

Experimental contents for characterization of MEL zeolites; the study of catalytic and diffusion performance of synthesized MEL zeolites; additional SEM, XPS, UV-vis, EPR,  $^{27}\text{Al}$  MAS NMR, FTIR, TEM,  $\text{N}_2$  isotherm data, TGA and GC-MS analysis.

## Acknowledgment

This work was supported by Natural Science Foundation of China (No. 21978055 and 21808040), the Science and Technology Program of Guangzhou, China (201804010172) and “High-level Talents Program” of Pearl River (2017GC010080). Y. Zhu acknowledges the financial support from the National Natural Science Foundation of China (Grant No. 21771161) and Thousand Talents Program for Distinguished Young Scholars.

## Literature Cited

1. Li B, Leng K, Zhang Y, et al. Metal–Organic Framework Based upon the Synergy of a Brønsted Acid Framework and Lewis Acid Centers as a Highly Efficient Heterogeneous Catalyst for Fixed-Bed Reactions. *J. Am. Chem. Soc.* 2015;137(12):4243-4248.
2. Huang J, Liu B, Liao Z, Chen H, Yan K. Fabrication of Cu-Encapsulated Hierarchical MEL Zeolites for Alkylation of Mesitylene with Benzyl Alcohol. *Ind. Eng. Chem. Res.* 2019;58(36):16636-16644.
3. Jin H, Ansari MB, Jeong E-Y, Park S-E. Effect of mesoporosity on selective benzylation of aromatics with benzyl alcohol over mesoporous ZSM-5. *J. Catal.* 2012;291:55-62.
4. Hwang YK, Chang J-S, Park S-E, et al. Microwave Fabrication of MFI Zeolite Crystals with a Fibrous Morphology and Their Applications. *Angew. Chem.Int. Ed.* 2005;44(4):556-560.
5. Yuan B, Li Y, Wang Z, Yu F, Xie C, Yu S. A Novel Brønsted-Lewis acidic catalyst based on heteropoly phosphotungstates: Synthesis and catalysis in benzylation of p-xylene with benzyl alcohol. *Mol. Catal.* 2017;443:110-116.
6. Pérez-Ramírez J, Christensen CH, Egeblad K, Christensen CH, Groen JC. Hierarchical zeolites: enhanced utilisation of microporous crystals in catalysis by advances in materials design. *Chem. Soc. Rev.* 2008;37(11):2530-2542.
7. Hartmann M, Machoke AG, Schwieger W. Catalytic test reactions for the evaluation of hierarchical zeolites. *Chem. Soc. Rev.* 2016;45(12):3313-3330.
8. Wei Y, Parmentier TE, de Jong KP, Zecevic J. Tailoring and visualizing the pore architecture of hierarchical zeolites. *Chem. Soc. Rev.* Oct 21 2015;44(20):7234-7261.
9. Liu B, Ren Y, Duan Q, Chen F, Xi H, Qian Y. Facile synthesis of mesoporous aluminosilicates constructed with crystalline microporous frameworks. *Appl. Surf. Sci.* 2013;279:55-61.
10. Dai C, Zhang A, Liu M, Gu L, Guo X, Song C. Hollow Alveolus-Like Nanovesicle Assembly with Metal-Encapsulated Hollow Zeolite Nanocrystals. *ACS nano.* 2016;10(8):7401-7408.
11. Pagis C, Morgado Prates AR, Farrusseng D, Bats N, Tuel A. Hollow Zeolite Structures: An Overview of Synthesis Methods. *Chem. Mater.* 2016;28(15):5205-5223.
12. Zhang F, Yan Y, Yang H, et al. Understanding Effect of Wall Structure on the Hydrothermal Stability of Mesoporous Silica SBA-15. *J. Phys. Chem. B.* 2005;109(18):8723-8732.
13. Zhu J, Zhu Y, Zhu L, et al. Highly Mesoporous Single-Crystalline Zeolite Beta Synthesized Using a Nonsurfactant Cationic Polymer as a Dual-Function Template. *J. Am. Chem. Soc.* 2014;136(6):2503-2510.

14. Zhang Q, Mayoral A, Terasaki O, et al. Amino Acid-Assisted Construction of Single-Crystalline Hierarchical Nanozeolites via Oriented-Aggregation and Intraparticle Ripening. *J. Am. Chem. Soc.* 2019;141(9):3772-3776.
15. Tao S, Li X, Wang X, et al. Facile Synthesis of Hierarchical Nanosized Single-Crystal Aluminophosphate Molecular Sieves from Highly Homogeneous and Concentrated Precursors. *Angew. Chem. Int. Ed.* 2020;59(9):3455-3459.
16. Milina M, Mitchell S, Crivelli P, Cooke D, Pérez-Ramírez J. Mesopore quality determines the lifetime of hierarchically structured zeolite catalysts. *Nat. Commun.* 2014;5(1):3922.
17. Zubiaga A, Warringham R, Boltz M, et al. The assessment of pore connectivity in hierarchical zeolites using positron annihilation lifetime spectroscopy: instrumental and morphological aspects. *Phys. Chem. Chem. Phys.* 2016;18(13):9211-9219.
18. Coq B, Gourves V, Figuéras F. Benzylolation of toluene by benzyl chloride over protonic zeolites. *Appl. Catal., A.* 1993;100(1):69-75.
19. Choudhary VR, Jana SK, Mamman AS. Benzylolation of benzene by benzyl chloride over Fe-modified ZSM-5 and H- $\beta$  zeolites and Fe<sub>2</sub>O<sub>3</sub> or FeCl<sub>3</sub> deposited on micro-, meso- and macro-porous supports. *Microporous Mesoporous Mater.* 2002;56(1):65-71.
20. Salavati-Niasari M, Hasanalian J, Najafian H. Alumina-supported FeCl<sub>3</sub>, MnCl<sub>2</sub>, CoCl<sub>2</sub>, NiCl<sub>2</sub>, CuCl<sub>2</sub>, and ZnCl<sub>2</sub> as catalysts for the benzylolation of benzene by benzyl chloride. *J. Mol. Catal. A: Chem.* 2004;209(1):209-214.
21. Knapp C, Obuchi A, Uchisawa JO, Kushiyama S, Avila P. Method for selective removal of supported platinum particles from external zeolite surfaces: characterisation of and application to a catalyst for the selective reduction of nitrogen oxide by hydrocarbons. *Microporous Mesoporous Mater.* 1999;31(1):23-31.
22. Wu Z, Goel S, Choi M, Iglesia E. Hydrothermal synthesis of LTA-encapsulated metal clusters and consequences for catalyst stability, reactivity, and selectivity. *J. Catal.* 2014;311:458-468.
23. Zhao X, Wang X. Characterizations and Catalytic Properties of Chromium Silicalite-2 Prepared by Direct Hydrothermal Synthesis and Impregnation. *Catal. Lett.* 2010;135(3-4):233-240.
24. Gomez S, Lerici L, Saux C, et al. Fe/ZSM-11 as a novel and efficient photocatalyst to degrade Dichlorvos on water solutions. *Appl. Catal., B.* 2017;202:580-586.
25. Tan P. Active phase, catalytic activity, and induction period of Fe/zeolite material in nonoxidative aromatization of methane. *J. Catal.* 2016;338:21-29.
26. Zhang D, Yang RT. N<sub>2</sub>O Formation Pathways over Zeolite-Supported Cu and Fe Catalysts in NH<sub>3</sub>-SCR. *Energy Fuels.* 2018;32(2):2170-2182.
27. Yang Y, Zhang H, Yan Y. The preparation of Fe<sub>2</sub>O<sub>3</sub>-ZSM-5 catalysts by metal-organic chemical vapour deposition method for catalytic wet peroxide oxidation of m-cresol. *Roy. Soc. Open. Sci.* 2018;5(3):171731.
28. Chen Y, Li C, Chen X, Liu Y, Tsang C-W, Liang C. Synthesis and Characterization of Iron-Substituted ZSM-23 Zeolite Catalysts with Highly Selective Hydroisomerization of n-Hexadecane. *Ind. Eng. Chem. Res.* 2018;57(41):13721-13730.
29. Pérez Vélez R, Ellmers I, Huang H, et al. Identifying active sites for fast NH<sub>3</sub>-SCR of NO/NO<sub>2</sub> mixtures over Fe-ZSM-5 by operando EPR and UV-vis spectroscopy. *J. Catal.* 2014;316:103-111.
30. Alzeer MIM, MacKenzie KJD, Keyzers RA. Facile synthesis of new hierarchical aluminosilicate inorganic polymer solid acids and their catalytic performance in alkylation reactions. *Microporous Mesoporous Mater.* 2017;241:316-325.

31. Yutthalekha T, Wattanakit C, Warakulwit C, et al. Hierarchical FAU-type zeolite nanosheets as green and sustainable catalysts for benzylation of toluene. *J. Clean. Prod.* 2017;142:1244-1251.
32. Abelló S, Bonilla A, Pérez-Ramírez J. Mesoporous ZSM-5 zeolite catalysts prepared by desilication with organic hydroxides and comparison with NaOH leaching. *Appl. Catal., A.* 2009;364(1):191-198.
33. Wang S, Wang P, Qin Z, et al. Relation of Catalytic Performance to the Aluminum Siting of Acidic Zeolites in the Conversion of Methanol to Olefins, Viewed via a Comparison between ZSM-5 and ZSM-11. *ACS Catal.* 2018;8(6):5485-5505.
34. Bleken F, Skistad W, Barbera K, et al. Conversion of methanol over 10-ring zeolites with differing volumes at channel intersections: comparison of TNU-9, IM-5, ZSM-11 and ZSM-5. *Phys. Chem. Chem. Phys.* 2011;13(7):2539-2549.
35. Lyu J-H, Hu H-L, Rui J-Y, et al. Nitridation: A simple way to improve the catalytic performance of hierarchical porous ZSM-5 in benzene alkylation with methanol. *Chin. Chem. Lett.* 2017;28(2):482-486.
36. Candu N, Florea M, Coman SM, Parvulescu VI. Benzylation of benzene with benzyl alcohol on zeolite catalysts. *Appl. Catal., A.* 2011;393(1-2):206-214.
37. Seo Y, Cho K, Jung Y, Ryoo R. Characterization of the Surface Acidity of MFI Zeolite Nanosheets by <sup>31</sup>P NMR of Adsorbed Phosphine Oxides and Catalytic Cracking of Decalin. *ACS Catal.* 2013;3(4):713-720.
38. Zhao Z, Li Z, Lin YS. Adsorption and Diffusion of Carbon Dioxide on Metal-Organic Framework (MOF-5). *Ind. Eng. Chem. Res.* 2009;48(22):10015-10020.
39. Li C, Ren YQ, Gou JS, Liu BY, Xi HX. Facile synthesis of mesostructured ZSM-5 zeolite with enhanced mass transport and catalytic performances. *Appl. Surf. Sci.* 2017;392:785-794.
40. Qi X, Vattipalli V, Dauenhauer PJ, Fan W. Silica Nanoparticle Mass Transfer Fins for MFI Composite Materials. *Chem. Mater.* 2018;30(7):2353-2361.
41. Emdadi L, Wu Y, Zhu G, et al. Dual Template Synthesis of Meso- and Microporous MFI Zeolite Nanosheet Assemblies with Tailored Activity in Catalytic Reactions. *Chem. Mater.* 2014;26(3):1345-1355.
42. Emdadi L, Oh SC, Wu Y, et al. The role of external acidity of meso-/microporous zeolites in determining selectivity for acid-catalyzed reactions of benzyl alcohol. *J. Catal.* 2016;335:165-174.
43. Mantri K, Komura K, Kubota Y, Sugi Y. Friedel-Crafts alkylation of aromatics with benzyl alcohols catalyzed by rare earth metal triflates supported on MCM-41 mesoporous silica. *J. Mol. Catal. A: Chem.* 2005;236(1):168-175.
44. Choudhary V, Jana S, Mamman A. Benzylation of benzene by benzyl chloride over Fe-modified ZSM-5 and H- $\beta$  zeolites and Fe<sub>2</sub>O<sub>3</sub> or FeC<sub>13</sub> deposited on micro-, meso- and macro-porous supports. *Microporous Mesoporous Mater.* 2002;56:65-71.
45. Trnik A, Scheinherrova L, Medved I, Cerny R. Simultaneous DSC and TG analysis of high-performance concrete containing natural zeolite as a supplementary cementitious material. *J Therm Anal Calorim.* 2015;121(1):67-73.
46. Gou J, Wang Z, Li C, et al. The effects of ZSM-5 mesoporosity and morphology on the catalytic fast pyrolysis of furan. *Green Chem.* 2017;19(15):3549-3557.
47. Li J, Xiang H, Liu M, Wang Q, Zhu Z, Hu Z. The deactivation mechanism of two typical shape-selective HZSM-5 catalysts for alkylation of toluene with methanol. *Catal. Sci. Technol.* 2014;4(8):2639-2649.
48. Liu Y, Zou Y, Jiang H, Gao H, Chen R. Deactivation mechanism of beta-zeolite catalyst for synthesis of cumene by benzene alkylation with isopropanol. *Chin. J. Chem. Eng.* 2017;25(9):1195-1201.